Numerical contact simulation of the mechanical interaction between a parameterized Stent frame model and Abdominal Aortic Aneurysms

Carsten Ditzel (Leibniz University Hannover - Germany)

Abstract
The treatment of Abdominal Aortic Aneurysms with the Endovascular aneurysm repair method has become more and more popular in the last decades due to its minimal-invasive nature and favourable long-term results. With the rapid improvement in available computational power and the progress in advanced numerical modelling of biomechanical processes and applications there is an increasing desire for fast, reliable and reproduceable simulations of stent-artery interactions prior to any surgical intervention. In the depicted scenario a stent implant comes into contact with a human artery in-vivo and therefore mechanical forces are to be taken into account and potential risk factors have to be estimated in order to predict the mechanical response correctly. Numerical simulations in this context can contribute to eliminate application failures and preclude fatal mistakes from the start. The present work deals with the numerical setup and subsequent simulation of the Stent Graft apposition inside an Aortic Aneurysm as well as the development of solution approaches to tackle the dynamic Stent-Aorta contact problem.

Contents

1. Physiological fundamentals

The aorta is the largest artery in the human body and transports blood with high oxygen content from the heart into the great circulatory system, thereby supplying almost the entire body with blood. It originates in the left ventricle of the heart from where it runs down to the abdomen after branching off into the renal arteries eventually bifurcating into two separate parts called the Common Iliac Arteries. The outer diameter within an adult person ranges between $25 - 35$ mm while its length averages from $300 - 400$ mm. Its highly elastic constitutive behaviour allows for providing a continuous stream of blood by internal pressure balancing as the blood flow generated by the heartbeat propagates down the artery in pulsatile waves. Therefore its mechanical characteristics are of utmost importance and already small morphological changes can have severe consequences regarding the reliable performance of the vessel and its vital functions.A rather common mutation of the Aortic vascular is the Abdominal Aortic Aneurysm (AAA) which constitutes irreversible progressive

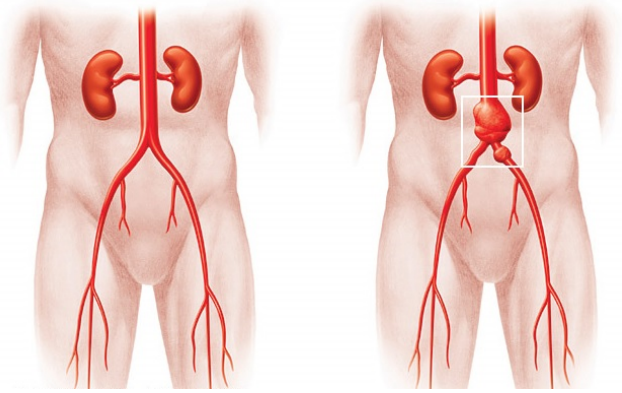

Figure 1. Healthy Aorta in contrast to Abdominal Aortic Aneurysm, taken from [1]

dilatations of the vessel between the two bifurcation points depicted in figure 1. The reasons for the development of these kinds of aortic degenerations are complex but research points towards environmental influences as well as genetic factors playing crucial roles in this context. Symptomatic for the appearance of AAAs if often the occurence of intra-luminal thrombi as well as the existence of calcifications within the vessel wall, leading to local stiffening and thus a reduction of the elastic response abilities of the artery. The overall resultant degradation of the material integrity of the artery, i.e. the local weakening of the aortic structure, accompanied by radial bulging of the geometry and deformed shape, increases the risk of life-threatening ruptures due to the enduring fluid

pressure within. As a remedy two options exist, with the first one being traditional open surgery and the second one being the so-called minimal-invasive endovascular aneurysm repair method (EVAR), which according to contemporary surveys exhibits slightly better chances of recovery and tends to lead to comparably lower mortality rates [2]. To this end a stenting procedure, utilizing a small metal-fabric tubular structure called Stent Graft, a catheter and a guide wire, is applied. Through an incision of a femoral artery opening out

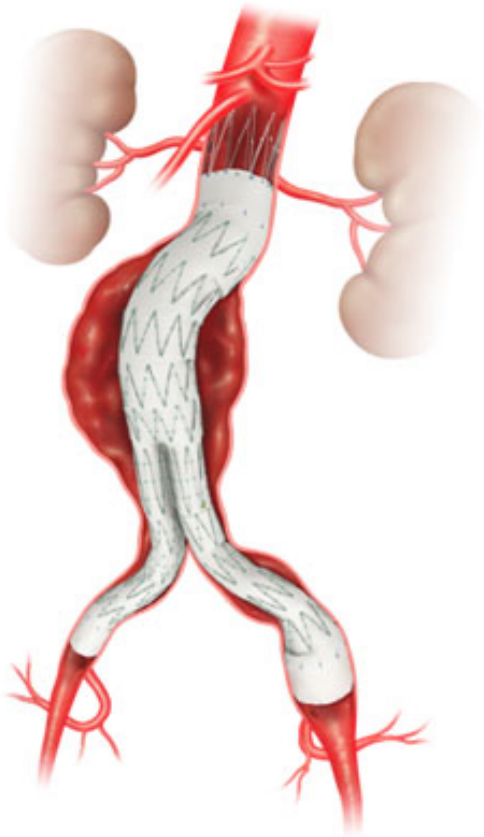

Figure 2. Deployed Stent Graft within AAA, taken from [3]

into the iliac artery the guide wire is introduced into the abdominal aorta along which the crimped Stent device enclosed by the catheter is advanced to the affected aneurysm area until just below the renal arteries. Composed of an impermeable polyester prosthesis and a supporting flexible self-expanding metal mesh (e.g. Nitinol), the retraction of the protective catheter causes the Stent Graft to unfold radially, bypassing the aneurysm and thus giving pressure relief to the artery wall while now retaining undisturbed blood flow through the Stent Graft scaffolding the artery. Subsequently, the further expansion of the Stent structure via inflation of an introduced balloon provides for a tight seal at the proximal and distal positions of the deployed Stent so that the risk of endoleaks is significantly reduced. This stage of the process is shown in illustration 2. After successful surgery, chances are the aneurysm will shrink and dilatations will decrease over time minimizing the danger of rupture.

While presenting a slightly smaller number of post intervention complications, the long-term mortality rate of EVAR, compared to the open surgical approach, has been reported to be quite similar [4]. Usually a combination of reasons is decisive for the minimal invasive method sometimes not being successful in the long run. Among these are problems with the physiological acceptance of the implant, degeneration of the stent material followed by a partial loss of the mechanical properties or failure of the geometrical structure. But also inflammations due to the insertion of a foreign object and the ensuing mechanically restricted physiological flexibility of the artery (Vasomotion) involve a certain amount of risk which can delay or hinder the process of health improvement.

The above mentioned aspects in total highlight the importance of a detailed and thorough investigation of the mechanical interaction between artery tissue and artificial implant. To facilitate those analyses, numerical simulations have become more and more essential in this particular biomedical field of application, not only because of their excellent result reproduction ability but also due to the apparent absence of extensive in vivo testing opportunities.

2. Computational contact mechanics

Contact mechanics, in its most general conception, comprises the determination of the mechanical response of two or more continuous bodies that partially come into physical contact as well as the description of the mutual interaction that is to be expected as time progresses. This process is depicted in figure 3 where two material points, associated with the boundaries of the bodies in the reference configuration, spatially occupy the same point in the current configuration, thus imposing further constraints on the systems behaviour. In

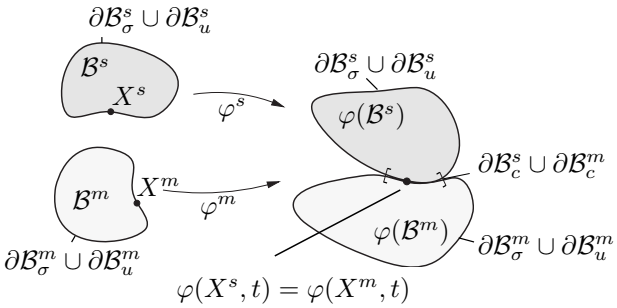

Figure 3. Finite deformation contact, mod. from [5]

addition to the bodies disjunct surfaces with prescribed displacements $\partial\mathcal{B}_u$ and surface tractions $\partial\mathcal{B}_\sigma$, a third area $\partial\mathcal{B}_c$ arises where contact boundary conditions have to be applied: As to this one has to distinguish between the occurence of normal and tangential contact, taking place along the normal

direction and in the tangential plane of the contact partners surface respectively. In this report only normal contact, i.e. frictionless investigations are considered for reasons given below. In the case of continua with locally convex surface regions every point on the surface of the so-called slave body $\boldsymbol{x}^s$ can be uniquely assigned a corresponding point on the master surface $\bar{\boldsymbol{x}}^m$ which exhibits the smallest relative distance as can be seen in figure 4. This leads to an optimization

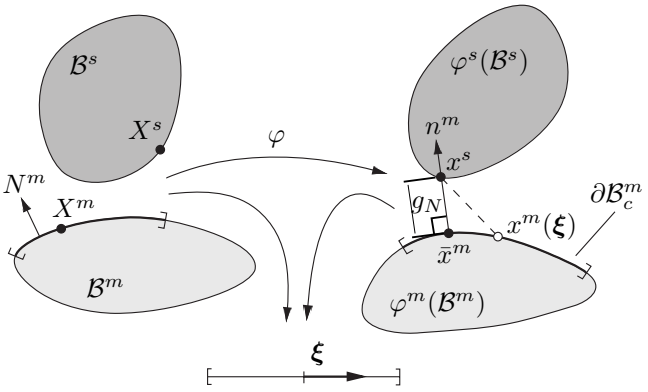

Figure 4. Minimum distance problem in deformed configuration, mod. from [5]

problem in which the closest specific position on the master surface that is usually parametrized by convective coordinates $\boldsymbol{\xi} = (\xi^1, \xi^2)$ is determined via

$$d(\xi^1, \xi^2) = \underset{\boldsymbol{x}^m \subseteq \Gamma_c^m}{\operatorname{argmin}} \, \|\boldsymbol{x}^s - \boldsymbol{x}^m(\boldsymbol{\xi})\| \tag{1}$$

$$\Rightarrow \quad \frac{\partial}{\partial \xi^\alpha} \, d(\xi^1, \xi^2) = \underbrace{\frac{\boldsymbol{x}^s - \boldsymbol{x}^m(\xi^1, \xi^2)}{\|\boldsymbol{x}^s - \boldsymbol{x}^m(\xi^1, \xi^2)\|}}_{\boldsymbol{d}} \cdot \underbrace{\boldsymbol{x}^m_{,\alpha}(\xi^1, \xi^2)}_{\boldsymbol{a}^m_\alpha} = 0. \tag{2}$$

The second factor $\boldsymbol{x}^m_{,\alpha}(\xi^1, \xi^2)$ here means the derivative with respect to one of the two convective coordinates, therefore yielding the tangential vectors to the surface $\partial\mathcal{B}_c^m$ in the direction of either ξ^1 or ξ^2. Since therefore the first factor has to point in the direction of the surface normal, the solution to these nonlinear perpendicularity conditions is the orthogonal projection of the slave point onto the current master surface represented by the set of convective coordinates $\bar{\xi}^1$ or $\bar{\xi}^2$. In certain situations there might be no unique solution to this problem, as in the case of locally non-convex surface parts, or even no solution at all, when regions are locally non-differentiable, as shown in graphic 5 below. While considering normal contact only, the necessary contact constraint is given by a pure geometric, yet nonlinear expression also called normal gap function which has to be fulfilled at all times, thereby preventing penetration of one body into the other.

$$g_N = \left[\boldsymbol{x}^s - \boldsymbol{x}^m(\bar{\boldsymbol{\xi}})\right] \cdot \boldsymbol{n}^m(\bar{\boldsymbol{\xi}}) \geq 0 \tag{3}$$

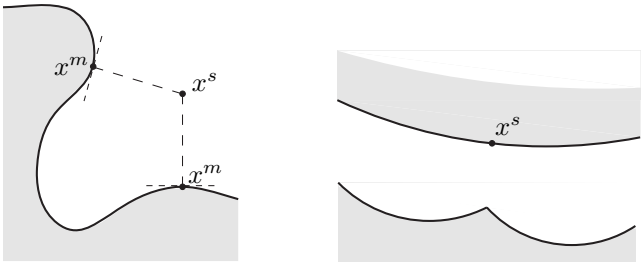

Figure 5. Problems in contact detection, mod. from [5]

Evaluating this dot product at the previously calculated projection point at which $\boldsymbol{n}^m(\bar{\boldsymbol{\xi}})$ is the outward unit normal on the master surface defined as

$$\boldsymbol{n}^m(\bar{\boldsymbol{\xi}}) = \frac{\boldsymbol{a}^m(\bar{\xi}^1) \times \boldsymbol{a}^m(\bar{\xi}^2)}{\|\boldsymbol{a}^m(\bar{\xi}^1) \times \boldsymbol{a}^m(\bar{\xi}^2)\|} \tag{4}$$

results in the effective distance between master and slave point, thus defining the local contact state. The normal gap function is used to specify the Hertz-Signorini-Moreau conditions as an equivalent to the Karush-Kuhn-Tucker conditions which are well known from mathematical optimization theory

$$g_N \geq 0 \qquad p_N \leq 0 \qquad g_N \, p_N = 0 \tag{5}$$

and state that the contact pressure p_N has to be zero for a positive gap value and yield a compressive contact stress for a closed gap, denoting contact between two bodies (compare [6]). The last condition is called strict complementarity because only one of both factors can be zero at the same time.

The most general and well established contact concept within the Finite Element framework including finite deformations is the node-to-surface discretization in which discrete slave nodes can come into contact with arbitrary master surface facets and even slide over several adjacent patches, (see [7]).

Choosing the principle of virtual work instead of an energy potential as a theoretical starting point does not preclude the incorporation of dissipative processes from the start. Following the notation used in [8], this yields

$$\sum_{\tau=m,s} \delta W^\tau_{\text{int}} = \sum_{\tau=m,s} \delta W^\tau_{\text{ext}} + \sum_{\tau=m,s} \delta W^\tau_{\text{ext,c}}. \tag{6}$$

The stress divergence term as well as the external virtual work for both contact partners in the current configuration are as usually defined as

$$\sum_{\tau=m,s} \delta W^\tau_{\text{int}} = \int_{B^\tau} \boldsymbol{\sigma}^\tau : \operatorname{grad} \delta\boldsymbol{u}^\tau \, \mathrm{d}v^\tau$$

and

$$\sum_{\tau=m,s} \delta W^{\tau}_{\text{ext}} = \int\limits_{B^{\tau}} \rho^{\tau}(\boldsymbol{b}^{\tau} - \boldsymbol{a}^{\tau}) \cdot \delta\boldsymbol{u}^{\tau} \,\mathrm{d}v^{\tau} + \int\limits_{\partial B^{\tau}\sigma} \boldsymbol{t}^{\tau} \cdot \delta\boldsymbol{u}^{\tau} \,\mathrm{d}a^{\tau}_{\sigma}$$

respectively and its derivation can be found e.g. in [9]. The additional term including the contact contribution that couples the interaction of both bodies is defined as

$$\sum_{\tau=m,s} \delta W^{\tau}_{\text{ext,c}} = \int\limits_{\partial B^{s}_{c}} \boldsymbol{t}^{s}_{N} \cdot \delta\boldsymbol{u}^{s} \,\mathrm{d}a^{s}_{c} + \int\limits_{\partial B^{m}_{c}} \boldsymbol{t}^{m}_{N} \cdot \delta\boldsymbol{u}^{m} \,\mathrm{d}a^{m}_{c}$$

and is based upon the assumption that the contact interface is known in every calculation step, which is ensured by the employment of an active set strategy within the numerical solution algorithms. Due to the enforcement of linear momentum along the contacting surfaces the normal contact traction $\boldsymbol{t}_N = p_N\,\boldsymbol{n}$, acting on both slave and master surface is equal but opposite in direction, i.e. $\boldsymbol{t}_N = \boldsymbol{t}^{s}_{N} = -\boldsymbol{t}^{m}_{N}$. Therefore the above equation can be shortened to

$$\sum_{\tau=m,s} \delta W^{\tau}_{\text{ext,c}} = \int\limits_{\partial B^{s}_{c}} \boldsymbol{t}_{N} \cdot [\delta\boldsymbol{u}^{s} - \delta\boldsymbol{u}^{m}] \,\mathrm{d}a^{s}_{c}$$

where in this case the integration is to be carried out over the slave surface. Employing the variation of the gap function

$$\delta g_N = \left[\delta\boldsymbol{x}^{s} - \delta\boldsymbol{x}^{m}(\bar{\boldsymbol{\xi}})\right] \cdot \boldsymbol{n}^{m}(\bar{\boldsymbol{\xi}}) \tag{7}$$

(details given in [10]) facilitates the reformulation of the integrand into the final form of the contact residuum which contributes to the right hand side of the global equation system as the summation over all active contact elements n_c

$$\sum_{\tau=m,s} \delta W^{\tau}_{\text{ext,c}} = \int\limits_{\partial B^{s}_{c}} p_N\,\delta g_N \,\mathrm{d}a^{s}_{c} \approx \sum_{s=1}^{n_c} p_{N_s}(\bar{\boldsymbol{\xi}})\,\delta g_{N_s}(\bar{\boldsymbol{\xi}})\,A_s. \tag{8}$$

In the above expression A_s represents the surface associated with the respective slave node. The contact pressure definition, however, depends upon the specific method selected to account for the contact constraints (see [11]) and - in the following employed penalty method - is $p_N = \epsilon_N\,g_N$ with $\epsilon_N > 0$. The penalty parameter ϵ_N serves as sort of an artificial spring stiffness trying to compensate the violation of the contact constraints and therefore has to be chosen carefully according to certain features of the underlying mechanical system.

The major advantage of this regularization method is the absence of additional degrees of freedom in the resulting system of equations in comparison to the Lagrangian multiplier method. On the other hand the most significant drawback is an only approximate fulfillment of the contact constraints where any increase of the penalty value leads indeed to improved results, but at the same time downgrades the condition number of the system matrix as described in [12].

The additional contribution to the tangential stiffness matrix resulting from the linearization of the internal and external forces is obtained by consistent linearization of the residual part (8)

$$\Delta\delta W^{\gamma}_{\text{ext,c}} = \epsilon_N \int\limits_{\partial B^{s}_{c}} \left[\Delta g_{N_s}\delta g_{N_s} + g_{N_s}\,\Delta(\delta g_{N_s})\right] \,\mathrm{d}a^{s}_{c}. \tag{9}$$

In this expression not only the linearization of the gap function is required which has the same structure as (7) giving

$$\Delta g_N = \left[\Delta\boldsymbol{u}^{s} - \Delta\boldsymbol{u}^{m}(\bar{\boldsymbol{\xi}})\right] \cdot \boldsymbol{n}^{m}(\bar{\boldsymbol{\xi}}) \tag{10}$$

but also the linearization of the variation of this function in the normal direction has to be inserted. Details of the derivation are given in [13] and are rather intricate in a sense that both the convective coordinates and the surface normal vector are depending on the displacement field and hence have to be accounted for during the linearization process. Here only the final result is stated in which $\boldsymbol{\eta}^{\tau} = \delta\boldsymbol{x}^{\tau}$ was set for abbreviation.

$$\begin{aligned}\Delta(\delta g_N) = &- \left[\bar{\boldsymbol{\eta}}^{m}_{,\alpha}\,\Delta\xi^{\alpha} + \Delta\bar{\boldsymbol{u}}^{m}_{,\alpha}\,\delta\xi^{\alpha} + \bar{\boldsymbol{x}}^{m}_{,\alpha\beta}\,\Delta\xi^{\beta}\,\delta\xi^{\alpha}\right] \cdot \bar{\boldsymbol{n}}^{m} \\ &+ g_N\,\bar{\boldsymbol{n}}^{m} \cdot \left[\bar{\boldsymbol{\eta}}^{m}_{,\alpha} + \bar{\boldsymbol{x}}^{m}_{,\alpha\beta}\,\delta\xi^{\beta}\right] \bar{a}^{\alpha\gamma} \left[\Delta\bar{\boldsymbol{u}}^{m}_{,\gamma} + \bar{\boldsymbol{x}}^{m}_{,\gamma\theta}\,\Delta\xi^{\theta}\right] \cdot \bar{\boldsymbol{n}}^{m}\end{aligned}$$

This equation is symmetric with respect to variation and linearization, thereby retaining symmetry of the overall tangent and maintaining quadratic convergence in the numerical algorithms used later to solve the resulting global system of equations. The subindices denote derivation or evaluation with respect to one of the convective coordinates whereas the quantities $\delta\bar{\xi}^{\alpha}$ and $\Delta\bar{\xi}^{\alpha}$ have to be determined through iteration processes by themselves. The bar again designates quantities that have to be evaluated at the respective projection points.

The discretization process followed here uses quadrilateral four-node elements to describe the contact surface of the underlying master body which itself is subdivided into hexahedral elements, described in [14]. This choice is most convenient as it makes use of the fact that the surface parametrization via convective coordinates is in this case equivalent to the isoparametric spatial approximation of the underlying mesh

([5]). The surface interpolation

$$\boldsymbol{x}^m(\xi^1,\xi^2) = \sum_{I=1}^{4} N_I(\xi^1,\xi^2)\,\boldsymbol{x}_I^m \tag{11}$$

with the Lagrangian shape functions

$$N_I = \frac{1}{4}(1-\xi_I^1\xi^1)(1-\xi_I^2\xi^2) \tag{12}$$

therefore allows for the following numerical procedure:
Assuming that contact surfaces which possibly may come into contact are known beforehand, a local contact detection phase is introduced after each iteration or alternatively after each load-/timestep of the simulation. Herein the closest master node to each slave node belonging to the contact interface is determined by simple distance calculations. Next, all element facets adjacent to those respective master nodes are examined in order to find the one that features the projection point. To this purpose the perpendicularity condition (2) has to be discretized

$$\left[\boldsymbol{x}^s - \sum_{I=1}^{4} N_I(\boldsymbol{\xi})\,\boldsymbol{x}_I^m\right] \cdot \sum_{K=1}^{4} N_{K,\alpha}(\boldsymbol{\xi})\,\boldsymbol{x}_K^m = 0. \tag{13}$$

As a consequence of the application of bilinear shape functions the interpolation across the element surface is in general non-linear. For this reason the closest points expressed by the natural coordinates which fulfill (13) have to be computed using an iterative scheme, locally for each slave node. The discretized form of the linearized projection equation (13) can be found in [5]. As a final step, input of the resulting solution coordinates into the discretized gap function

$$g_N = \left[\boldsymbol{x}^s - \sum_{I=1}^{4} N_I(\bar{\boldsymbol{\xi}})\,\boldsymbol{x}_I^m\right] \cdot \boldsymbol{n}^m(\bar{\boldsymbol{\xi}}) \tag{14}$$

enables one to determine whether contact for a specific node-segment pair is active or not. In the first case the contribution of this five-node contact element to the global system of equation has to be accounted for to introduce forces that counteract the existing constraint violations. To this end, the discretization of the residuum and stiffness part, i.e. equations (8) and (9) respectively then result in the following expressions

$$R_{c_s} = \sum_{s=1}^{n_c} \boldsymbol{\eta}_s^T p_{N_s} \boldsymbol{N}_s A_s \tag{15}$$

$$\Delta\, R_{c_s}(\boldsymbol{x},\boldsymbol{\eta}) \cdot \Delta\boldsymbol{u} \approx \sum_{s=1}^{n_c} A_s\, \boldsymbol{\eta}_s^T \boldsymbol{K}_{c_s}\, \Delta\boldsymbol{u}_s$$

where

$$\boldsymbol{\eta}_s^T = [\boldsymbol{\eta}^s,\ \boldsymbol{\eta}_1^m,\ \boldsymbol{\eta}_2^m,\ \boldsymbol{\eta}_3^m,\ \boldsymbol{\eta}_4^m]$$

is the vector of displacement variations associated with the s-th active contact element and

$$\Delta\boldsymbol{u}_s^T = [\Delta\boldsymbol{u}^s,\ \Delta\boldsymbol{u}_1^m,\ \Delta\boldsymbol{u}_2^m,\ \Delta\boldsymbol{u}_3^m,\ \Delta\boldsymbol{u}_4^m]$$

is the vector of incremental contact nodal displacements of that very same element. The expression

$$\begin{aligned}\boldsymbol{K}_{c_s} &= \epsilon_N \left[\boldsymbol{N}_s\boldsymbol{N}_s^T + g_N\,\Delta(\delta g_{N_s})\right] \\ &= \epsilon_N \left[\boldsymbol{N}_s\boldsymbol{N}_s^T + g_N \left[\boldsymbol{N}_\alpha \boldsymbol{D}_s^{\alpha T} + a^{\beta\alpha}\boldsymbol{T}_\alpha\left(\boldsymbol{N}_\beta^T - \boldsymbol{D}_s^{\gamma T}(\bar{\boldsymbol{n}}^m\cdot\bar{\boldsymbol{a}}_{\beta,\gamma}\right)\right]\right]\end{aligned}$$

represents the contact stiffness contribution for one nodal pair in which $a^{\alpha\beta}$ denotes the metric tensor. The following discretization matrices have been used

$$\boldsymbol{N}_s = \begin{bmatrix} \bar{\boldsymbol{n}}^m \\ -N_1\,\bar{\boldsymbol{n}}^m \\ -N_2\,\bar{\boldsymbol{n}}^m \\ -N_3\,\bar{\boldsymbol{n}}^m \\ -N_4\,\bar{\boldsymbol{n}}^m \end{bmatrix}, \boldsymbol{N}_\beta = \begin{bmatrix} \boldsymbol{0} \\ -N_{1,\beta}\,\bar{\boldsymbol{n}}^m \\ -N_{2,\beta}\,\bar{\boldsymbol{n}}^m \\ -N_{3,\beta}\,\bar{\boldsymbol{n}}^m \\ -N_{4,\beta}\,\bar{\boldsymbol{n}}^m \end{bmatrix}, \boldsymbol{T}_\beta = \begin{bmatrix} \bar{\boldsymbol{a}}_\alpha \\ -N_1\,\bar{\boldsymbol{a}}_\beta \\ -N_2\,\bar{\boldsymbol{a}}_\beta \\ -N_3\,\bar{\boldsymbol{a}}_\beta \\ -N_4\,\bar{\boldsymbol{a}}_\beta \end{bmatrix}$$

as well as

$$\boldsymbol{D}_s^\alpha = H^{\alpha\beta}\left[\boldsymbol{T}_\beta - g_{N_s}\boldsymbol{N}_\beta\right]$$

where $H^{\alpha\beta} = \left[\bar{a}_{\alpha\beta} + g_{N_s}\bar{b}_{\alpha\beta}\right]^{-1}$ includes the curvature tensor $\bar{b}_{\alpha\beta}$ that accounts for changes in the orientation of element surfaces. The resulting global system of linear equations to be solved at the current displacement state is finally given by

$$\left[\boldsymbol{K}_T(\bar{\boldsymbol{u}}) + \boldsymbol{K}_c(\bar{\boldsymbol{u}})\right]\,\Delta u = -\left[\boldsymbol{G}(\bar{\boldsymbol{u}}) + \boldsymbol{R}_c(\bar{\boldsymbol{u}})\right].$$

3. Modelling and Assumptions

The focus of this project lies on the simulation of the deployment of a Stent Graft device within an Abdominal Aortic Aneurysm. Therefore several steps have to be taken into account to set up an appropriate model suitable for the intended numerical calculations. First, the patient-specific physiology, i.e. the geometry of the respective area inside the human body has to be captured. This is usually done via CT- or MRT scans and then processed by means of image processing algorithms in order to get a spatial and computationally applicable set of data. Based on this information the morphology of the Aorta is reconstructed and eventually subdivided into a finite number of elements. All these steps, including the meshing of the Aneurysm, are in the present study performed by the

software *A4clinics-Research Edition*™ [15] which in the latest version also allows for the generation of an input file that can be read in by the Finite Element program *FEAP* [16]. The result is a three-dimensional mesh of the aortic aneurysm consisting of three distinctive parts, namely the vessel wall and the intra-luminal thrombus discretized by eight-node brick elements as well as the lumen, i.e. the interior surface area of the artery described by quadrilaterals. These different element partitions share common nodes at specific locations and thus form one single discrete body, however each with possibly different constitutive behaviour. The basic buildup is presented in graphic 6 below.

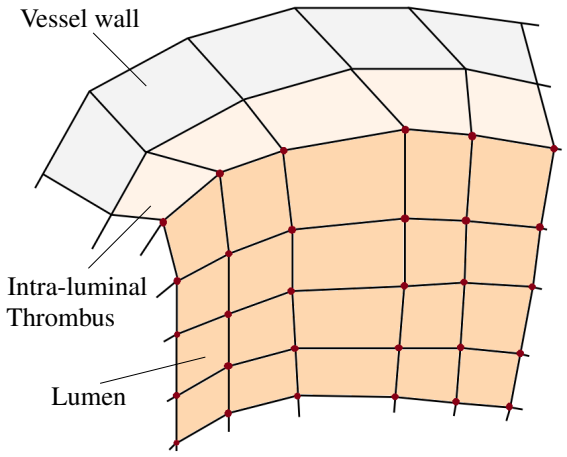

Figure 6. Topological composition of the vascular layers

Especially the separate consideration and calculational treatment of the influence of the Intra luminal Thrombus has been shown to be of significant importance [17], when investigating mechanical responses of living vessels like e.g. wall-stresses and changing dimensions.

Accounting for the nearly incompressible material behaviour of vascular tissue is also essential, as has been shown before in e.g. [18]. Therefore specific user-material models implemented into FEAP by T.C. Gasser were used to describe the natural characteristics with a compromise of accuracy and mumerical convenience. These routines employ a mixed Q1P0 element formulation and assume a hyperelastic, homogeneous, isotropic Yeoh strain energy density function neglecting the cubic term.

$$W = a_1 (I_b - 3) + a_2 (I_b - 3)^2$$

Moreover, additional augmentations were used in order to enforce the isochore properties of the vessel tissue. The identification of the particular material parameters used here for the different parts of the vascular model is described in the papers of Raghavan and Vorp for the vessel wall [19] and Vande Geest, Sacks and Vorp for the Thrombus respectively [17]. The respective material data is listed in table 1 below.

It should be noted, however, that Arterial walls are naturally extremely anisotropic media because of the structured arrangement of the load-carrying collagen fiber components within its walls. The chosen material model therefore presents an approximation to the actually much more complicated constitution.

Vascular part	a_1 [MPa]	a_2 [MPa]	$\rho\,[^{kg}/_{mm^3}]$
Vessel wall	0.174	1.881	$1e-6$
Thrombus	0.00798	0.00871	$1e-6$

Table 1. Constitutive vascular parameters

The entire simulation procedure described below takes place in a finite deformation framework, since large displacements and large rotations are taking place. For the design and generation of the implant consisting of a bifurcated metal Stent, several assumptions have to be made concerning the choice of elements as well as the selection of the constitutive data used within the following calculations. Furthermore, the overall dimensions are to be adapted to the respective shape and size of the obtained patient-specific Artery morphology. To this end several Matlab Scripts were written and combined in a graphical user interface to not only extend and modify the mesh data imported from the *A4clinics-Research Edition*™ but also adjust the generated Stent to loosely fit the topology of the aorta in a first attempt. To begin with, a certain AAA-geometry has to be selected from the library after which the Stent model is generated accordingly and the entire input file is created by using prescribed simulation parameters.

Illustration 7 not only shows the lumen discretized by four node quadrilateral elements and designated to serve as the master surface of the selected AAA but also the Stent mesh as well as the bifurcated common Illiac mesh part in the initial undeformed configuration. Only contact surface elements of the AAA are displayed to facilitate a clear overview. The basic model set up is consequently composed of three individual bodies.

- Abdominal Aortic Aneurysm
- Main Stent
- Iliac Stent

The Iliac Stent and the Main Stent share the same layout but differ in dimensions and longitudinal location. All depicted Stent nodes are defined as slave nodes that can potentially come into contact with the lumen surface. In view of the already quite large number of nodes and elements the complete Aortic Aneurysm model consists of and due to the inherent spatial structure of a metallic Stent device, two-node 3D-Bernoulli beam-elements were used to create the implant. The applicability of beam elements in this context is reported in [20]. To further limit the amount of unknowns in the problem,

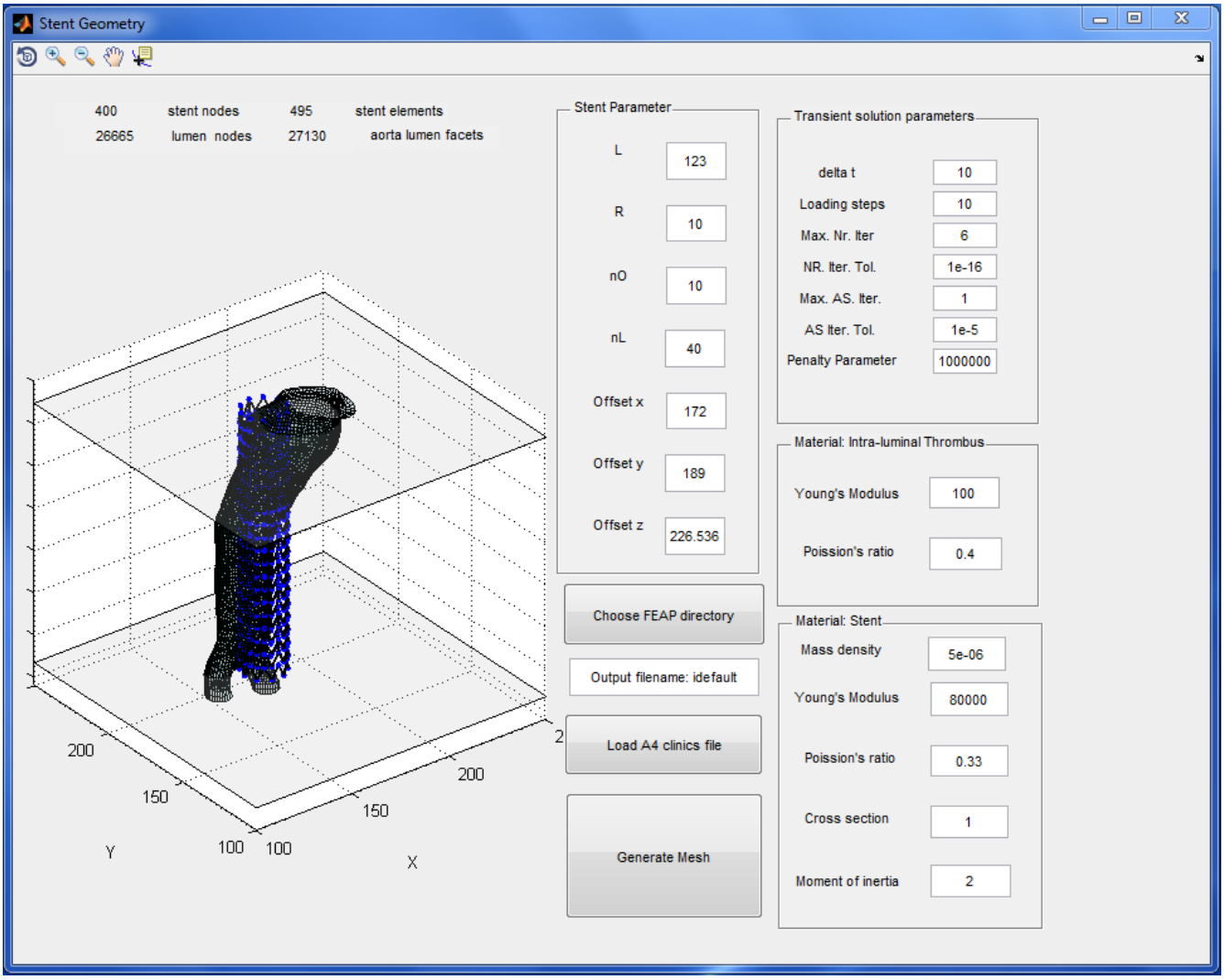

Figure 7. GUI with selected AAA lumen surface, adapted Stent geometry and choice of simulation parameters

an explicit modelling of the fabric was neglected, also because the main structural rigidity is provided by the metal frame (see [21]) whose interaction with the tissue is the main focus here. Every node of the frame mesh has six degrees of freedom (3 translations and 3 rotations) and the cross-section was selected to be circular for the entire model. The particular nodal interconnections were chosen in conformance to Aortic Stent layouts that can be found in the literature, e.g. [22]. Different Stent designs were initially considered as depicted in figure 8, where only the main Stent layouts are displayed for illustrational purposes. These frame structures vary by nodal number, nodal positions and element connections and thus exhibited considerably different flexibility unter compression, extension and deflection. Finally a fourth layout shown in figure 9 was chosen because of its comparatively low resistance to bending movements when exposed to lateral forces and its similarity to existing AAA Stent Graft devices. The underlying mathematical formulation for the spatial generation of the Stent nodes is oriented on [23] and reads for the individual vector function components

$$
\begin{aligned}
n(1)_{i,j} &= R\,\cos\left((i-1)\;\phi + (j-1)\;\phi/2\right)\\
n(2)_{i,j} &= R\,\sin\left((i-1)\;\phi + (j-1)\;\phi/2\right)\\
n(3)_{i,j} &= \begin{cases} (j-1)\;{}^{L}/_{n_L}, & \text{if } j \text{ is odd and } j \neq n_L\\ (j-1)\;{}^{L}/_{n_L} + {}^{L}/_{n_L}, & \text{if } j \text{ is even} \end{cases}
\end{aligned}
$$

where $\boldsymbol{n}_{i,j}$ describes one vertex location and $i = 1, \ldots, n_O$ denotes the indices of the nodes in the circumferential direction whereas $j = 1, \ldots, n_L$ are the nodal indices in the longitudinal Stent direction. R is the radius and $\phi = 2\pi/n_O$ describes the circumferential nodal resolution of the structure.

Due to the specifically chosen mesh description the number of nodes n_O at inner Stent levels is twice the number of nodes at the bottom and top layers. This fact also dictates the choice of n_L to be an even number and influences the

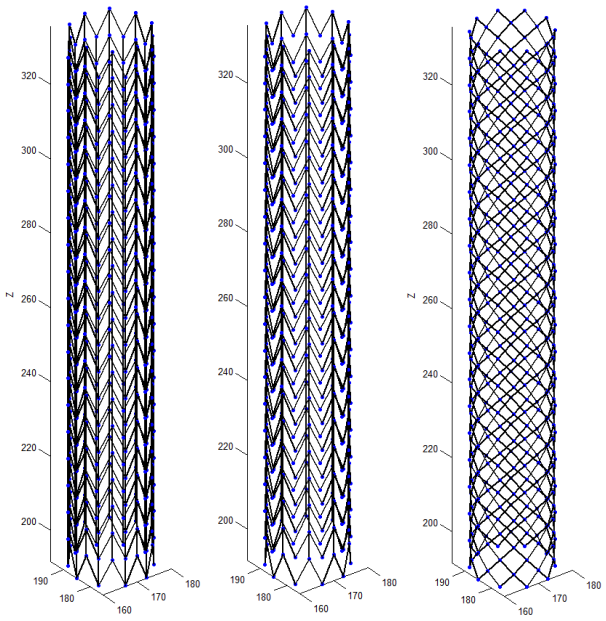

Figure 8. Primary metal frame topologies

overall number of axial levels of nodes so that the final number is ${}^{n_L}/_2 + 1$ which results in a uniform geometry for the Stent. The specific algorithm for the generation of the nodes and the element connections is given in Appendix A. The number of circumferential nodes (n_O) and axial nodes (n_L) can be varied in the GUI rendering the geometrical Stent behaviour more soft or more stiff in radial and axial direction respectively. In this study a circumferential nodal resolution of $n_O = 10$ and a radial node number of $n_L = 40$ have been chosen. Also the radius of the Stent tube in the undeformed configuration can be chosen. However, by default and in agreement with clinical practice, it is initially set to be 30% larger then the proximal neck diameter of the Aorta to give a tight seal after self-expansion and to prevent any possible forms of Endoleakage. As a next step, suitable material parameters for the entire Stent device have to be selected. In the context of vessel interventions Nitinol stents are widely used due to their superelastic properties, good corrosion resistance and biocompatibility. By assuming the metal structure to be homogeneous and isotropic this selection is therefore reduced to the choice of Young's modulus and Poisson's ratio. Specific values have been taken from published data (e.g. [24]) and are shown in table 2 below.

After selecting appropriate solution parameters, namely time

Stent	E [MPa]	ν	$\rho\ [{}^{kg}/_{mm^3}]$
Nitinol	80000	0.33	$5e-6$

Table 2. Constitutive Stent parameters

increments, number of time/-loading steps, maximal number of Newton-Raphson and Active-Set iterations as well as

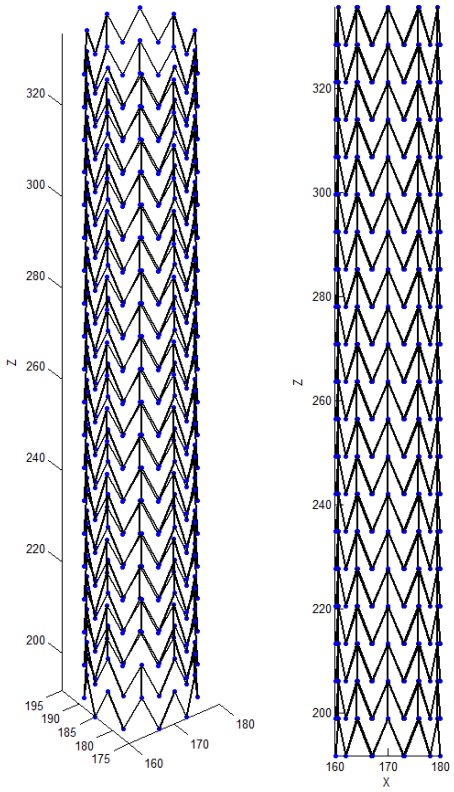

Figure 9. Final metal frame design

their respective tolerances, the Penalty parameter has to be adjusted. As mentioned before this choice is of utmost importance, since it affects the numerical stability of the entire contact simulation. The respective choice of this value mainly depends on the stiffness of the model and was chosen to $1000000\ N/mm^2$ to account for the rather high differences in material rigidity of the contact partners.

As mentioned before only normal contact is investigated here as the stent device expands radially inside the lumen, primarily exposing the wall to indentation until the final deployment state is reached. The abstinence of the fabric that usually mainly contributes to the frictional effects also justifies this assumption.

By reading in an *A4clinics*-file, the GUI then identifies a geometric centerline inside the aortic lumen that is later on used for the fitting process between Stent and Aorta. Due to the irregular mesh of the lumen surface its identification, however, proved to be a challenging task, especially in the regions of the Common Illiac Arteries where the bifurcation is located. An example of the implemented centerline calculation is given in figure 10 and also displays the scanning points along the centerline axis that are later on used for the adaption process of the implant.

The number of these discrete points depends on the number of Stent node levels chosen before in the axial direction, so that every node along the Stent length can be uniquely as-

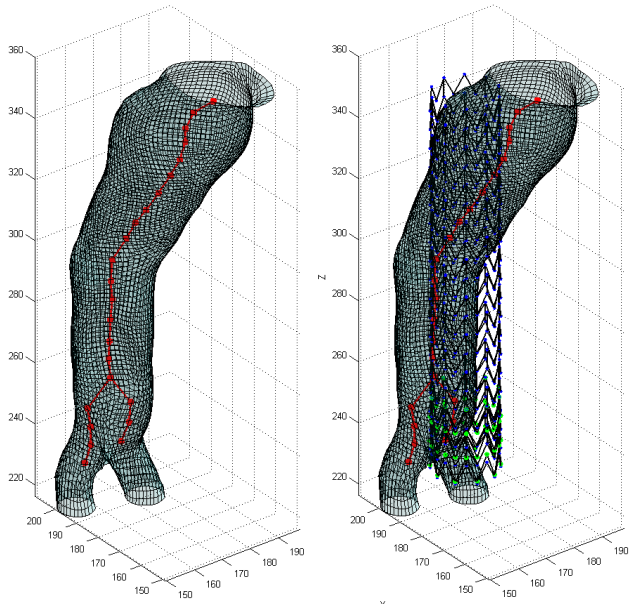

Figure 10. Centerline inside the lumen of an AAA and Stent adjustment

signed an corresponding centerline point for the upcoming initial adapting phase of the simulation. The program also adjusts the axial Stent length accordingly and a vertical shift if performed to align vessel and implant in the axial direction, which is shown on the right side of figure 10. As it turned out, these steps are rather crucial to obtain a convergent solution:

First trial runs based merely on the initial model setup, in which the normal contact penalty parameter was gradually increased in order to force the oversized Stent structure successively inside the Aorta, diverged rapidly when the provided Aorta geometry was highly deformed and locally deflected. In this scenario several slave nodes were initially be located far outside the defined master surface which led to vast gap function values, eventually causing the resulting system of equations to be ill-conditioned, thereby aborting the calculation.

Another attempt to drive the Stent nodes of the undeformed mesh to corresponding positions located circularly around the centerline before activating the contact constraints was also discarded: The topological characteristics of the Stent structure make it prone to buckling when adjacent nodes are moving in certain, e.g. opposite directions, thus resulting in an unstable state of the system before the actual contact simulation has even set in.

4. Simulation

Consequently, an alternative solution procedure was devised that comprises four main phases resembling to some extent the procedure presented in [24], so that the approach to this contact boundary value problem can be described as follows.

1. **Crimping** of the undeformed Stent structure radially towards its center
2. **Shifting** the Stent nodes to their respective positions along the aortic centerline
3. **Merging** the main Stent mesh and the Iliac part by linking designated connecting nodes
4. **Unfolding** the compressed Stent tube while activating contact

This course of action clearly differs from the reality in which the folded Stent is shoved to the region of interest from below the Iliac ateries but was chosen here due to numerical stability reasons. The final mesh data of the particular AAA and the Stent device within the performed simulation are illustrated in table 3 below.

Mesh	Nodes	Dof/Node	Elements	Dof/Elem.
AAA	5371	3	3918	24
Cont. surf.	1545	3	1522	12
Main Stent	400	6	495	12
Illiac Stent	100	6	120	12

Table 3. Mesh data of the simulation

4.1 Crimping

The first part closely mimicks reality in that it also relies on an incipient folding of the Stent frame before any deployment inside the vessel. However, the catheter - naturally enfolding the compressed Stent - was not included in the performed simulations. As pointed out earlier, the main reason for incorporating this initial step in the computation prior to any contact considerations is to reduce the overall risk of buckling. To compress the Stent, boundary conditions were imposed at

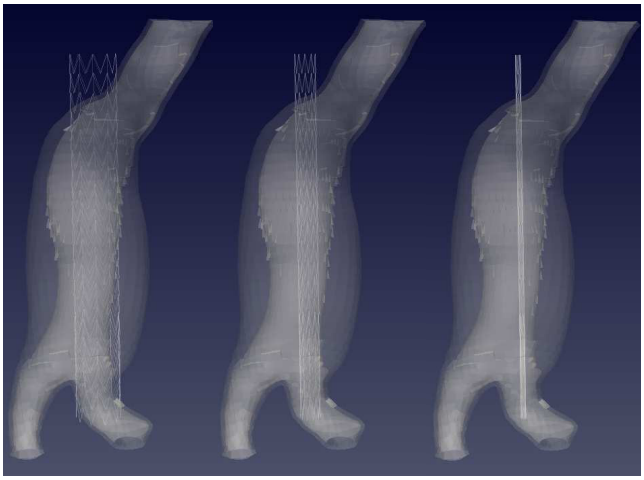

Figure 11. Crimping of the Stent and Illiac part

every frame node for every degree of freedom followed by a gradual quasistatic prescription of displacements in the X- and Y-cartesian coordinate directions, thereby driving the nodes radially in the middle until they almost completely coincide. During this step the Z-direction of the Stent nodes as well as the nodal rotations are fixed. Although this seems to be a rather drastic measure, the whole calculation is based on pure elastic material behaviour which makes the entire process path-independent and thus the final result valid as a starting point for the following simulation steps. The pre- and past compressing states of both, the Main and Iliac Stent part are illustrated in figure 11. During the compression of the Stent frame any contact detection is disabled and all nodes of the AAA are fixed to reduce computational costs.

4.2 Shifting

The second step involves the process of making the crimped Stent bodies coincide with the determined bifurcated centerline within the lumen. The shift is carried out by subdividing the relative distance between the nodal points and the centerline positions and driving the nodes dynamically to their designated positions in the X- and Y-direction within a couple of time steps. This fitting procedure is indicated in figure 12. Early experiments to also adjust the node positions in the Z-coordinate direction along the centerline imposed too many restraints on the system, so that the subsequent relaxation of the model in the fourth phase showed extensive deformations in the longitudinal direction even with relatively small time steps. The resulting internal stresses along the beam axis led

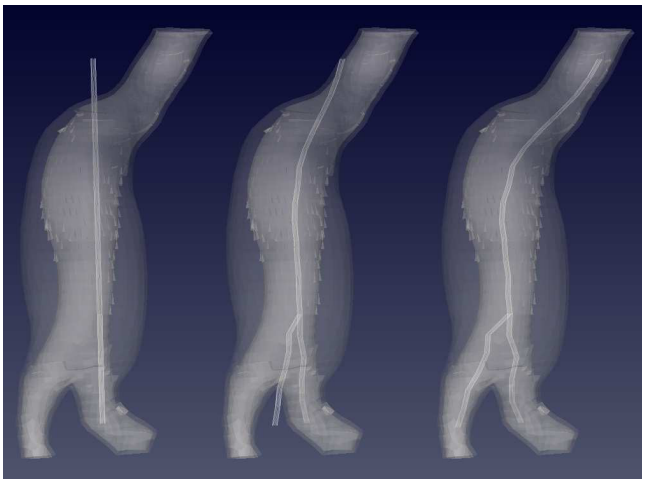

Figure 12. Adjustment of the Stent and the centerline

to considerable violations of the contact constraint equations at the beginning of the next steps in the simulation since single nodes consequently pierced deeply into the vessel wall, so that this approach was not pursued any further. In particluar, these observations emphasise the significance of an accurate and uniform determination of the centerline for the success of the subsequent contact calculations, so that the Stent mesh is not distorted and twisted too severely before the upcoming contact computations. As before, in this step all AAA nodes also remain fixed, rendering the Aneurysm model rigid and thereby decreasing the computational effort drastically.

4.3 Merging

Upon completion of the second phase the top nodes of the Iliac Stent part have the same positions as the nodes of the Main Stent which mark the branching point of the Stent structure. Nodes that coincided before in the undeformed configuration by radial angle are then linked together so that henceforth all six degrees of freedom of those specific nodal points are coupled. This step establishes the final connection between the Illiac part and the main body of the Stent and reduces the number of independent bodies within the simulation from three to two.

4.4 Unfolding

Prior to this final step of the simulation, all boundary conditions of the Stent are removed except for a remaining fixation of the top nodes in the Z-direction. Almost all AAA mesh nodes are released now as well, keeping restraints only at the distal and proximal sections in all three spatial directions, as indicated in figure 13. This excludes rigid body motions and prevents a singular system of equations. The stored elas-

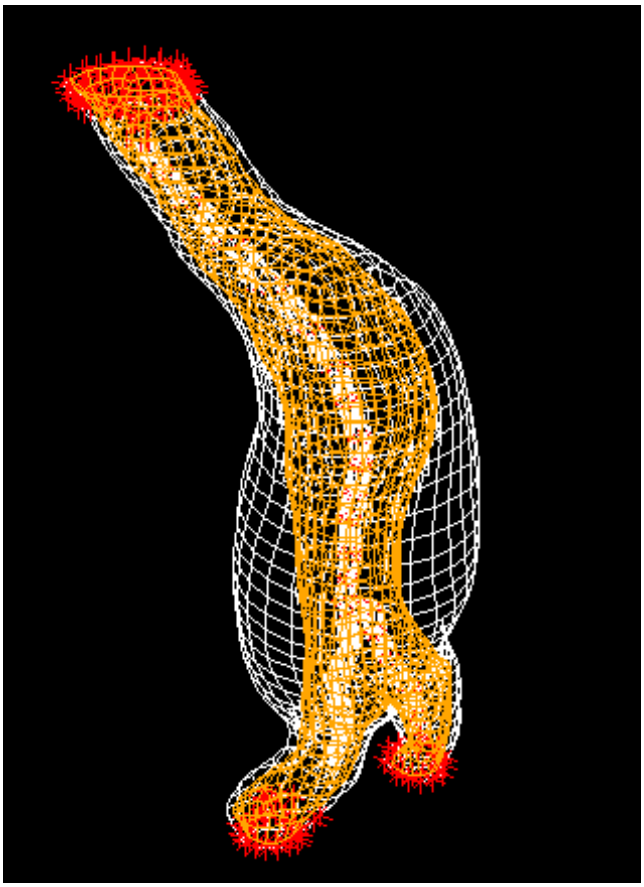

Figure 13. Final model constitution before contact calculations

tic energy within the structure due to the prior crimping and the sudden release of the Stents boundary conditions after being placed inside the AAA lumen now causes the metal frame to extend radially, thereby imitating the retraction of the catheter and the subsequent self-expansion of the structure during an EVAR procedure. This step is performed in a dynamic context by means of Newmark's implicit time-integration method. Because of the rather high compression of the beam-elements prior to this step and due to the fact that the release happens rapidly, a comparatively high global damping was introduced by specifying two Rayleigh damping coefficients to $\alpha = 500000000$ and $\beta = 50000000$. Especially the first, mass proportional factor adds some artificial ambient viscosity to the unfolding motion of the system so that the time increment can be chosen reasonably high. The continuum elements were fully integrated with two Gaussian points in every spatial direction and the nodes belonging to the lumen discretization are assigned an additional nodal-based damping associated with every degree of freedom to partially absorb the impact of the expanding frame. This turned out to be rather crucial in order to obtain global convergence in the course of the simulation although the determination of the nodal damping values was to some extent a process of trial and error.

5. Results and Interpretation

Illustration 14 shows the von Mises stresses in the vessel wall after 1500 seconds of contact simulation, i.e. after the dynamic release of the stent nodes with a strut radius of 1 mm. Since the focal point here lies on the mechanical response of the AAA rather than on the constitutional state within the Stent, the interval of the displayed stresses was scaled down and limited for demonstration purposes. The loading within the beam-elements due to the preceding compression is many magnitudes higher than inside the vessel wall and so the stent mesh uniformly appears in dark red.

As might be expected, the maximum stresses occur in the Illiac Section right below the bifurcation. Not only because here the lumen become naturally more narrow, but also due to the fact that the radius of the present simplified Stent model is not adapted, i.e. decreased in the Illiac parts in contrast to reality. Moreover, at these very locations, penetrations of wireframe elements through the vessel wall can be observed which is a major disadvantage of the node to surface contact approach in general and a result of too coarse a slave discretization in particular.

The literature reports finer discretized frame models of the wireframe rings via spline-fitting and the use of Timoshenko beam-elements which allows for a more precise local contact detection at the cost of a drastic increase in computational time (see [25]). Figure 15 displays a cut-through of the artery along the centroid of the lumen and therefore also reveals the stress distribution across the AAA wall. Especially the stress gradients at the interface between Thrombus and exterior vessel wall in sections of maximum Thrombus development

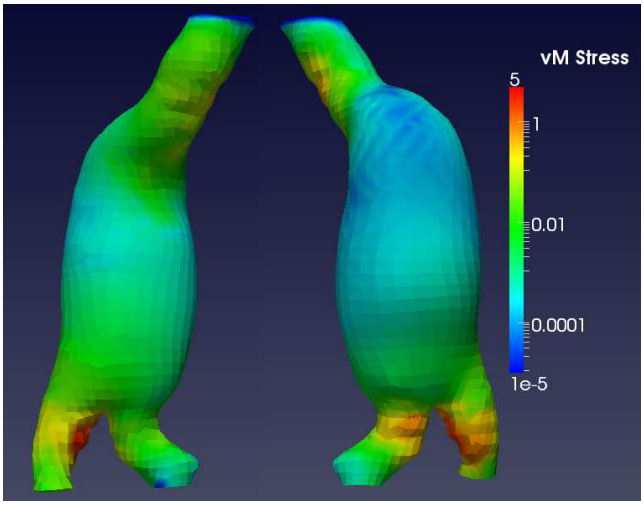

Figure 14. v. Mises stress state in the stented AAA with a strut radius of 1 mm

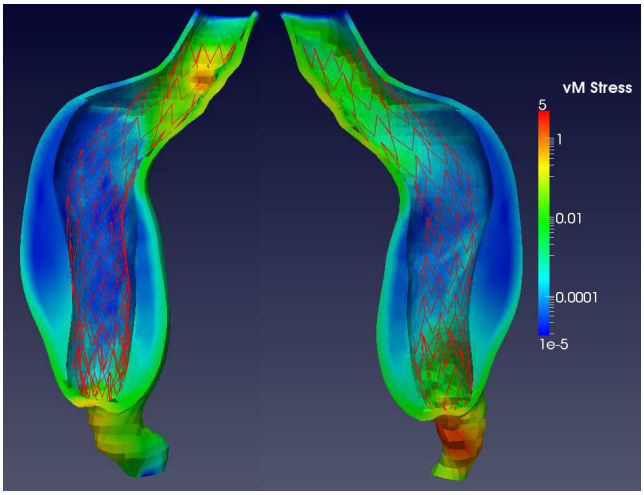

Figure 15. v. Mises stress state in AAA (cut-through) with a strut radius of 1 mm

are evident and clearly disclose the vast respective differences in the constitution of the material. Furthermore, the stress peak near the proximal neck of the Aorta due to local asymmetric deflections of the artery geometry underlines the sensitive reaction of the vessel tissue to the implant and highlights the importance of patient-tailored Stent Grafts and careful subsequent appositions. Otherwise, the high rigidity of the metal structure in comparison to the soft tissue material is cause for an increased risk of tissue pinching and damaging, which was demonstrated and confirmed by Liang et al. [26].

To estimate the influence of the rigidity of the metal frame in terms of the loading imposed on the vessel tissue, another simulation was performed in which the stent strut radius was decreased from 1 mm to 0.8 mm. As a result, a lower stress state within the wireframe model after compression and thus smaller radial forces are to be expected and consequently a

slower behaviour in radial expansion. This can be confirmed by the illustration in figure 16 which shows the von Mises stress state after the same simulation time than before. Not only is the overall stress distribution in the artery wall lower which is clearly visible with reference to 15 but also the radial extension has not progressed so far to make the stent struts touch the vessel wall completely in the regions of the proximal neck which could induce the development of endoleaks. This danger has been proved before in [27] using finite element analysis and highlights a very important point of the apposition of Stent Grafts within an AAA in general:

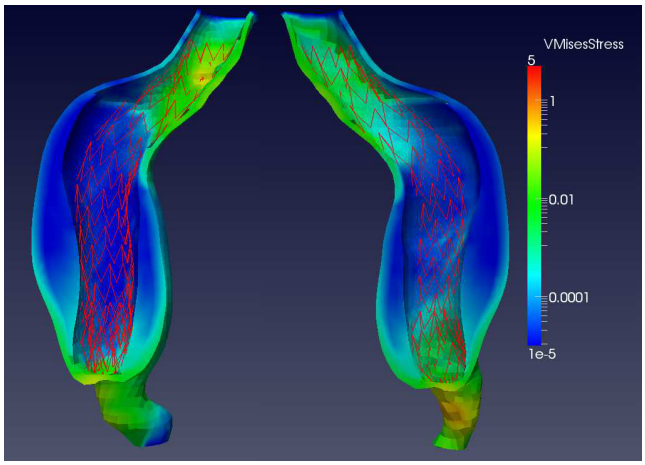

Figure 16. v. Mises stress state in AAA (cut-through) with a strut radius of 0.8 mm

A compromise always has to be made between preventing overstretching of the vessel neck and avoidance of injuries such as wall degeneration and neck dilatations on the one hand and maintaining sufficient contact and thus sealing between both media on the other hand to prevent e.g. endoleaking. The magnitude of the radial force exhibited by the expanding Stent is a key parameter in this regard and should in any case be high enough to support the vessel and anchor the Stent graft at the AAA neck ([22]).

6. Limitations and Outlook

Several assumptions and simplifications have been made in the present study, partly to limit the computational effort but also due to time restrictions.

Resorting to beam-elements to model the Stent structure is efficient and its validity had been proved before as reported in the literature. Nevertheless this choice of discretization does preclude some detailed mechanisms that take place at the interface between artery wall and implant. Wu et. al. [28] also sub-divide the stent structure with continuum elements and introduce frictional effects, thereby rendering the problem tremendously more expensive from a calculational point of view. With regard to the existing computational power, this choice confines the size of the investigated model and also allows for only relatively small parts of the biomechanical setting to be modelled explicitly. For the very same reasons the fabric material the stent struts are usually sewed onto was disregarded in the present study, although this is reported to have quite a significant impact on the expansion behaviour of the Stent Graft after retraction of the catheter by holding individual struts in place. In fact, the tendency of single strut nodes to pierce deeply inside the lumen wall was one of the main reasons why not only extremely high damping had to be introduced in the test runs but also comparatively small time steps were necessary to obtain convergence. As pointed out earlier, the intersection of elements with tissue is an unphysical drawback of the simulation but is due to the chosen contact discretization technique.

The constant radius of the wireframe model along its axis is a result of the applied vector function and is partially responsible for the enhanced stresses in the Illiac parts of the Aorta. This design choice should be revised in future works. The selected numerical apposition approach of the Stent could also be reassessed to make it more realistic and to simulate the real delivery inside the vessel and subsequent retraction of the catheter.

The pulsating blood pressure, usually modelled as a constant mean arterial pressure of 100 mmHg (13.3 kPa) was completely ignored. Partly because of the absence of the impermeable textile the blood will start to flow through after a successful apposition. But also the fact that the contact stresses are expected to be much higher than the flow-induced pressure was a deciding argument in this matter.

In conclusion, finite element applications in the biomedical field of Abdominal Aortic Aneurysms can assist in the design of new devices, identify valuable mechanical characteristics of the contact interaction between artery and Stent and contribute to the process of interpreting clinically obtained data. Systematic approaches and subsequent carefully performed parameter studies may lead to the development of patient-specific Stent designs with a minimized risk of post-invasive complications.

Appendix A

```
function [STENT] = genStent(L, R, nO, nL, ...
    shift_x, shift_y, shift_z )
%-----------------------------------------
% Generation of stent geometry by means of ...
    nodes and elements
% @C. Ditzel Dec. 2013
%-----------------------------------------
% input:
%   L:          Initial length of stent
%   R:          Initial radius of stent
%   nO:         Number of nodes in ...
    circumferential direction
%   nL:         Number of nodes in axial ...
    direction
%   shift_...:  Shift of the stent in the ...
    respective coordinate direction
%
% output:
```

```
%   STENT.nodes:      Matrix of nodal ...
    coordinates of the stent
%   STENT.elements:   Connectivity matrix ...
    of stent elements

global NUMNODES numel noelem
I = 1:nO;
J = 1:nL;
phi = 2*pi/nO; % resolution
STENT.nodes_init = zeros(nO*nL,3);
for i = 1 : length(I)
  for j = 1 : length(J)
       STENT.nodes_init(j + (nL)*(i-1), 1) ...
           = R*cos((I(i)-1)*phi + ...
           (J(j)-1)*(phi/2));
       STENT.nodes_init(j + (nL)*(i-1), 2) ...
           = R*sin((I(i)-1)*phi + ...
           (J(j)-1)*(phi/2));
    if (mod (j,2) ~= 0 && j ~= nL+1)
       STENT.nodes_init(j + (nL)*(i-1), 3) ...
           = (J(j)-1)*(L/nL);
    elseif (mod (j,2) == 0)
       STENT.nodes_init(j + (nL)*(i-1), 3) ...
           = (J(j)-1)*(L/nL)+(L/nL);
    end
  end
end

numNo = length( STENT.nodes_init);
% Element connections ascending
STENT.elements = [1:numNo; ...
    circshift(1:numNo,[-1 -1])]';
% Remove every seconds connection
STENT.elements(2:2:end,:) = [];
% Add the second part of elements
STENT.elements(length ...
    (STENT.elements)+1:length( ...
    STENT.elements)*2, :)
= [2:2:length( ...
    STENT.nodes_init);circshift(1:2:length( ...
    STENT.nodes_init),[-nL/2 -nL/2])]';

%% Weak stiffness model
% Choose even node numbers only for ...
    intermediate ring connections
n = [2:2:length( STENT.nodes_init)];
% Adjust seconds row of nodes for element ...
    connections
n = [n; circshift( n, [(nL-2)/2 (nL-2)/2])]';
% Remove top to bottom node connections
n = n(mod ( n(:,1), nL) ~= 0, :);
% Initialize logical vector to extract ...
    unwanted verticlal elements
logical = repmat([ones( (nL-2)/2,1); ...
    zeros( (nL-2)/2,1)], nO/2, 1);
% Remove unwanted vector entries by ...
    elementwise multiplication with logical
% vector
n = n( find( n(:,1).*logical),:);
% Complete elemente vector
STENT.elements(length ( ...
    STENT.elements)+1:length( ...
    STENT.elements) + length( n), :) = n;

STENT.nodes_init;
STENT.nodes(:,1) = STENT.nodes_init(:,1) + ...
    shift_x;
STENT.nodes(:,2) = STENT.nodes_init(:,2) + ...
    shift_y;
STENT.nodes(:,3) = STENT.nodes_init(:,3) + ...
    shift_z;
STENT.nodes;
```

Appendix B

```
function [offset_x, offset_y, offset_z, L, ...
    R, centroid_centerline, ...
    centroid_centerline_dist, ...
    centroid_iliac_centerline, ...
    centroid_iliac_centerline_dist, ...
    L_iliac, nL_iliac, offset_z_illiac, ...
    lumen_damping] =  morphing( AORTA, nL)
%-----------------------------------------
% morph stent geometry onto aorta ...
    geometric centerline
% @C. Ditzel Dec. 2013
%-----------------------------------------
%  input:
%   AORTA: Nodes and Connectivity matrix ...
    of intra-luminal surface elements
%
%
%  output:
% offset_...:                    Shift of ...
    the stent in the respective coordinate ...
    direction
% L_...:                         Length ...
    adjustment of stent according to ...
    geometry of Aorta
% R_...:                         Radial ...
    adjustment of stent according to ...
    proximalneck dimensions
% centroid_centerline_...:       Geometric ...
    centerline inside the lumen
% centroid_centerline_dist_...:  Length of ...
    geometric centerline
% lumen_damping:                 Extract ...
    lumen nodes for nodal damping assignment

% Extract all nodenumbers that are ...
    associated with elements of the
% intra-luminal Thrombus, sort them and ...
    remove multiples in the resultant vector
search = unique( sort( ...
    [AORTA.INTRA_LT(:,4), ...
    AORTA.INTRA_LT(:,5), ...
    AORTA.INTRA_LT(:,6), ...
    AORTA.INTRA_LT(:,7)]));
lumen_damping = search;
% Sort node numbers of intra-luminal ...
    Thrombus by ascending z-coordinate
Z_ascending = sortrows( AORTA.COORDS( ...
    search, 3:5), 3);

% Loop over the Z-coordinate of all lumen ...
    nodes for identification of
% center patch at bifurcation point
elemnodes = zeros( size( ...
    AORTA.INTRA_LT,1), 4);
for i = 1:size( AORTA.INTRA_LT,1)
    elemnodes(i,1) = AORTA.COORDS( ...
        AORTA.INTRA_LT(i,4), 5);
    elemnodes(i,2) = AORTA.COORDS( ...
        AORTA.INTRA_LT(i,5), 5);
    elemnodes(i,3) = AORTA.COORDS( ...
        AORTA.INTRA_LT(i,6), 5);
```

```
    elemnodes(i,4) = AORTA.COORDS( ...
        AORTA.INTRA_LT(i,7), 5);
end

% determine the flattest surface element ...
    by substracting the Z-coordinate of
% diagonal nodes of all quadrilateral ...
    surface elements and finding the
% smallest sum of both absolute values
[MIN_Z, Imin_Z] = min( abs( elemnodes(:,1) ...
    - elemnodes(:,3)) + ...
    abs( elemnodes(:,2) - elemnodes(:,4)));

% Get the x-/y-/z-coordinate of all four ...
    nodes of the flattest surface element
x = [AORTA.COORDS( AORTA.INTRA_LT( Imin_Z, ...
    4), 3);
    AORTA.COORDS( AORTA.INTRA_LT( Imin_Z, ...
        5), 3);
    AORTA.COORDS( AORTA.INTRA_LT( Imin_Z, ...
        6), 3);
    AORTA.COORDS( AORTA.INTRA_LT( Imin_Z, ...
        7), 3)];

y = [AORTA.COORDS( AORTA.INTRA_LT( Imin_Z, ...
    4), 4)
    AORTA.COORDS( AORTA.INTRA_LT( Imin_Z, ...
        5), 4)
    AORTA.COORDS( AORTA.INTRA_LT( Imin_Z, ...
        6), 4)
    AORTA.COORDS( AORTA.INTRA_LT( Imin_Z, ...
        7), 4)];

z = [AORTA.COORDS( AORTA.INTRA_LT( Imin_Z, ...
    4), 5)
    AORTA.COORDS( AORTA.INTRA_LT( Imin_Z, ...
        5), 5)
    AORTA.COORDS( AORTA.INTRA_LT( Imin_Z, ...
        6), 5)
    AORTA.COORDS( AORTA.INTRA_LT( Imin_Z, ...
        7), 5)];

%% Start position of Stent in the centroid ...
    of the whole artery
mid = sum( Z_ascending, 1)/size( ...
    Z_ascending, 1);

offset_x = round( mid(1,1));
offset_y = round( mid(1,2));

% scan_sections = floor(linspace( 1, size( ...
    Z_ascending, 1), size( Z_ascending, ...
    1)/100))
scan_sections = floor( linspace( min( ...
    Z_ascending(:,3) + 15), max( ...
    Z_ascending(:,3)), nL/2+2))
for i = 1:length( scan_sections) - 1
    centerline = ...
        Z_ascending(Z_ascending(:,3) ≥ ...
        scan_sections(i) & ...
        Z_ascending(:,3) < ...
        scan_sections(i+1), :);
    centroid_centerline(i,:) = sum( ...
        centerline, 1)/size( centerline, 1);
end

% Calculate initial neck diameter for ...
    radial dimension of stent, by
% increasing it by 30 %
tol_radius = 5;
R = Z_ascending(Z_ascending(:,3) ≤ ...
    scan_sections(end) & Z_ascending(:,3) ≥...
     scan_sections(end-1) + tol_radius, :);
Radius_x = max( R(:,1)) - min( R(:,1));
Radius_y = max( R(:,2)) - min( R(:,2));
R = floor( (max( Radius_x, Radius_y)*1.3)/2);

% Relative distance of scanned z coordinates
distance = diff( scan_sections)

% Distance from smallest z-coordinate of ...
    lumen to the aortic bifurcation point
iliac_dist = max( z) - min( Z_ascending(:,3))
nL_iliac = round( iliac_dist/distance(1)) ...
    + 2;

% Subsitute first 'nL_iliac' centerline ...
    entries by Iliac centroid values
for i = 1:nL_iliac
   centerline = ...
       Z_ascending(Z_ascending(:,3) ≥ ...
       scan_sections(i) & Z_ascending(:,3) ...
       < scan_sections(i+1) & ...
       (Z_ascending(:,1) < min( x) ), :);
   centroid_centerline(i,:) = sum( ...
       centerline, 1)/size( centerline, 1);

   centerline_iliac = ...
       Z_ascending(Z_ascending(:,3) ≥ ...
       scan_sections(i) & Z_ascending(:,3) ...
       < scan_sections(i+1) & ...
       (Z_ascending(:,1) > min( x)), :);
   centroid_iliac_centerline(i,:) = sum( ...
       centerline_iliac, 1)/size( ...
       centerline_iliac, 1);
end

% Substitute z-coordinate bei scanning values
centroid_centerline(:,3) = ...
    scan_sections(1:end-1);

% Substitute last row by main centerline ...
    entries
centroid_iliac_centerline(end,:) = ...
    centroid_centerline( ...
    length(centroid_iliac_centerline)+1,:);

% Calculate the piecewise linear length of ...
    the centerline
for i = 1:length( centroid_centerline)-1
    centroid_centerline_dist(i) = norm( ...
        centroid_centerline(i+1,:) - ...
        centroid_centerline(i,:));
end

% Adjust the height and length of the stent
L = max( centroid_centerline(:,3)) - min( ...
    centroid_centerline(:,3));
offset_z = min( Z_ascending(:,3)) + ((max( ...
    Z_ascending(:,3)) - min( ...
    Z_ascending(:,3))) - L)/2;


% Calculate the piecewise linear length of ...
    the iliac centerline
for i = 1:length( centroid_iliac_centerline)-1
    centroid_iliac_centerline_dist(i) = ...
        norm( ...
        centroid_iliac_centerline(i+1,:) - ...
        centroid_iliac_centerline(i,:));
```

```
113 end
114 L_iliac = sum( ...
        centroid_iliac_centerline_dist);
115 offset_z_illiac =  ...
        centroid_centerline(round( ...
        iliac_dist/distance(1))+3, 3) - L_iliac;
```

References

[1] http://www.aorticstents.com/. http://aorticstents.com/what-is-abdominal-aortic-aneurysm/. 2014.

[2] Sun Y. Endovascular stent graft repair of abdominal aortic aneurysms: Current status and future directions. *World Journal of Radiology*, 1:63–71, 2009.

[3] http://http://www.ipaustralia.gov.au/. http://www.ipaustralia.gov.au/images/listing-items/case-studies/zenithflexwithzenithspiralzlimbsanatomy.jpg. 2014.

[4] Greenhalgh R. Comparison of endovascular aneurysm repair with open repair in patients with abdominal aortic aneurysm (evar trial 1), 30-day operative mortality results: randomised controlled trial. *http://www.thelancet.com*, 364:843–848, 2004.

[5] P. Wriggers. Computational contact mechanics. *Springer*, 2006.

[6] T. Laursen. Computational contact and impact mechanics. *Springer*, 1. Edition, 2002.

[7] Konyukhov A. Schweizerhof K. Computational contact mechanics - geometrically exact theory for arbitrary shaped bodies. *Springer*, 1. Edition, 2013.

[8] Kiousis D. E. Gasser T. C. Holzapfel G. A. Smooth contact strategies with emphasis on the modeling of balloon angioplasty with stenting. *International journal for numerical methods in engineering*, 75:826–855, 2008.

[9] P. Wriggers. Nonlinear finite element methods. *Springer*, 2008.

[10] Yastrebov V. Numerical methods in contact mechanics. *Wiley*, 1. Edition, 2013.

[11] Nackenhorst U. Kontaktmechanik. *Institut fÄ ur Baumechanik und Numerische Mechanik*, 2006.

[12] Nasdala L. Fem-formelsammlung statik und dynamik. 1. Auflage, 2010.

[13] Yastrebov V. A consistent tangent stiffness matrix for three-dimensional non-linear contact analysis. *International Journal for Numerical Methods in Engineering*, 28:1803–1812, 1989.

[14] Zienkiewicz O. Taylor R. The finite element method: Volume 1 - the basis. *Butterworth - Heinemann*, 5. Edition, 2000.

[15] Auer M. Gasser T. C. Reconstruction and finite element mesh generation of abdominal aortic aneurysms from computerized tomography angiography data with minimal user interactions. *IEEE Transactions on medical imaging*, 29:1022–1028, 2010.

[16] Taylor R. Feap - a finite element analysis program. *University of California - Berkeley*, Version 8.4 - User Manual, 2013.

[17] Vande Geest J. Sacks M. Vorp D. A planar biaxial constitutive relation for the luminal layer of intra-luminal thrombus in abdominal aortic aneurysms. *Journal of Biomechanics*, 39:2347–2354, 2006.

[18] Carew T. Vaishnav R. Patel D. Compressibility of the arterial wall. *Circulation research*, 23:61–68, 1968.

[19] Raghavan M. Vorp D. Toward a biomechanical tool to evaluate rupture potential of abdominal aortic aneurysm: identification of a finite strain constitutive model and evaluation of its applicability. *Journal of Biomechanics*, 33:475–482, 2000.

[20] Zhao S. Gu L. Froemming S. Finite element analysis of the implantation of a self-expanding stent : Impact of lesion calcification. *Mechanical and Materials Engineering Faculty Publications*, University of Nebraska - Lincoln, 2012.

[21] Chen D. Conti M. Müller-Eschner M. Rengier F. Kotelis D. Böckler D. Ventikos Y. Xu Y. Zeng Y. Peng Y. Tengg-Kobligk H. A preliminary study of fast virtual stent-graft deployment: Application to stanford type b aortic dissection. *International Journal of Advanced Robotic Systems*, 2013.

[22] Kleinstreuer C. Basciano Z. Seelecke S. Farber M. Computational mechanics of nitinol stent grafts. *Journal of Biomechanics*, 41:2370–2378, 2008.

[23] Tambaca J. Kosor M. Canic S. Paniagua D. Mathematical modeling of vascular stents. *Society for Industrial and Applied Mathematics*, 70:1922–1952, 2010.

[24] Auricchio F. Conti M. De Beule M. De Santis G. Verhegghe B. Carotid artery stenting simulation: From patient specific images to finite element analysis. *Medical Engineering and Physics*, 33:281–289, 2011.

[25] Miguel A. Peirano M. Hernan G. Size of the proximal neck in aaas treated with balloon-expendable stent grafts. *Journal of the mechanical behaviour of biomedical materials*, 13:129–139, 2012.

[26] M. Wang W. Liang D. Yang D. Qi. Finite element analysis of the implantation of a balloon-expandable stent in a stenosed artery. *International Journal of Cardiology*, 104:314–318, 2005.

[27] Amblard A. Berre H. Bou Said B. Brunet M. Delivery and release of nitinol stent in carotid artery and their interactions: A finite element analysis. *Medical Engineering and Physics*, 31:27–33, 2009.

[28] Wu W. Qi M. Xiao-Peng L. Yang D. Wang W. Delivery and release of nitinol stent in carotid artery and their interactions: A finite element analysis. *Journal of Biomechanics*, 40:3034–3040, 2007.